

# Ion-Conductive, Viscosity-Tunable Hexagonal Boron Nitride Nanosheet Inks

Ana C. M. de Moraes, Woo Jin Hyun, Jung-Woo T. Seo, Julia R. Downing, Jin-Myoung Lim, and Mark C. Hersam\*

Liquid-phase exfoliation of layered solids holds promise for the scalable production of 2D nanosheets. When combined with suitable solvents and stabilizing polymers, the rheology of the resulting nanosheet dispersions can be tuned for a variety of additive manufacturing methods. While significant progress is made in the development of electrically conductive nanosheet inks, minimal effort is applied to ion-conductive nanosheet inks despite their central role in energy storage applications. Here, the formulation of viscosity-tunable hexagonal boron nitride (hBN) inks compatible with a wide range of printing methods that span the spectrum from low-viscosity inkjet printing to high-viscosity blade coating is demonstrated. The inks are prepared by liquid-phase exfoliation with ethyl cellulose as the polymer dispersant and stabilizer. Thermal annealing of the printed structures volatilizes the polymer, resulting in a porous microstructure and the formation of a nanoscale carbonaceous coating on the hBN nanosheets, which promotes high wettability to battery electrolytes. The final result is a printed hBN nanosheet film that possesses high ionic conductivity, chemical and thermal stability, and electrically insulating character, which are ideal characteristics for printable battery components such as separators. Indeed, lithium-ion battery cells based on printed hBN separators reveal enhanced electrochemical performance that exceeds commercial polymer separators.

## 1. Introduction

2D materials have attracted significant attention in recent years due to their diverse electronic, optical, thermal, and mechanical properties, which make them versatile building blocks for a range of applications.<sup>[1,2]</sup> The superlative properties of


2D materials arise from their covalently bonded in-plane structure and out-of-plane quantum confinement in addition to their high surface area to volume ratios that render them highly sensitive to surface stimuli.<sup>[1,3]</sup> For example, the in-plane structure of graphene is a covalently bonded honeycomb lattice of carbon atoms with  $sp^2$  hybridization, resulting in long-range  $\pi$ -conjugation and high electron mobility.<sup>[4,5]</sup> On the other hand, despite being a structural isomorph of graphene consisting of boron and nitrogen atoms in an analogous honeycomb structure, hexagonal boron nitride (hBN) is electrically insulating, which makes it an appealing dielectric for electronic applications.<sup>[6–13]</sup> In addition, hBN has excellent mechanical robustness and high thermal conductivity,<sup>[14]</sup> which has been utilized to enhance heat transport in composite materials<sup>[15–18]</sup> and nanofluids.<sup>[19,20]</sup>

In an effort to produce large quantities of 2D nanosheets, liquid-phase exfoliation has emerged as a leading method to exfoliate bulk layered crystals in solution.<sup>[21]</sup> In this approach, the energy required for exfoliation is introduced by ultrasonication or shear-mixing in organic solvents, aqueous surfactant media, ionic liquids, salts, or polymer solutions.<sup>[22,23]</sup> With appropriate solvents and additives, reaggregation of the exfoliated nanosheets is minimized, leading to stable dispersions<sup>[24]</sup> that can then be deposited onto substrates for thin-film applications.<sup>[22,25–27]</sup> When the rheology of these nanosheet dispersions is further controlled, they can be engineered into inks that are compatible with additive manufacturing technologies such as inkjet printing, screen printing, spray coating, and blade coating.<sup>[28]</sup> Since 2D nanosheets present intrinsic mechanical flexibility, printed nanosheet thin films are compatible with a variety of flexible and stretchable substrates.<sup>[25]</sup>

Despite these advantages, printable hBN nanosheet inks are still an emerging area of study with relatively few reports in the literature.<sup>[29]</sup> One of the rare examples is the development of a high-viscosity screen-printable hBN nanosheet ink that can be utilized as a printed dielectric.<sup>[30]</sup> Similarly, a fully inkjet-printed 2D material field-effect transistor was recently demonstrated, where the hBN ink was used to construct the gate dielectric layer.<sup>[29]</sup> However, printed hBN nanosheets possess

Dr. A. C. M. de Moraes, Dr. W. J. Hyun, Dr. J.-W. T. Seo, J. R. Downing, Dr. J.-M. Lim, Prof. M. C. Hersam  
Department of Materials Science and Engineering  
Northwestern University  
2220 Campus Drive, Evanston, IL 60208, USA  
E-mail: m-hersam@northwestern.edu

Prof. M. C. Hersam  
Department of Chemistry  
Department of Medicine, and Department of Electrical and Computer Engineering  
Evanston, IL 60208, USA

 The ORCID identification number(s) for the author(s) of this article can be found under <https://doi.org/10.1002/adfm.201902245>.

DOI: 10.1002/adfm.201902245

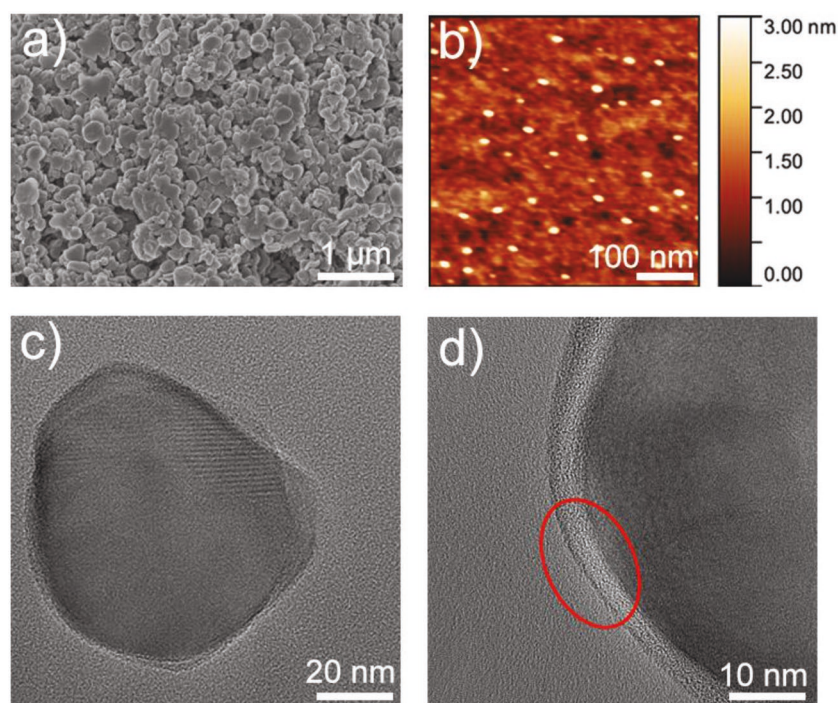


**Figure 1.** Morphology of hBN nanosheets exfoliated from bulk hBN in ethanol/EC by shear mixing. a) SEM image of the exfoliated hBN/EC powder. b) Individual hBN nanosheets observed by AFM. c,d) TEM images of exfoliated hBN nanosheets showing the EC coating on the surface of the nanosheets at (c) lower and (d) higher magnification.

limited competitive advantage compared to other printable dielectrics for electronics, suggesting the need for alternative hBN nanosheet ink formulations that are designed for other application areas.

In the arena of energy storage applications, lithium-ion batteries have increasing demands for printed components.<sup>[31,32]</sup> For instance, the battery separator is the component that physically prevents electrical contact between the anode and cathode while facilitating ion transport. This functionality requires printed structures that are concurrently electrically insulating and ionically conductive.<sup>[33]</sup> In principle, hBN meets the first requirement, but the second requirement necessitates a nanoporous hBN network that effectively absorbs battery electrolytes, thereby providing facile ion transport. Therefore, control over porosity and electrolyte wettability is required for printed hBN thin films to be effective in this context.<sup>[34]</sup>

Here, we address this unmet need for porosity control and electrolyte wettability by incorporating multifunctional cellulosic polymers into printable hBN inks. In particular, ethyl cellulose (EC) is employed to promote liquid-phase exfoliation and stabilization of hBN nanosheets in solution in a manner that is analogous to graphene nanosheets.<sup>[35–37]</sup> In addition to minimizing nanosheet reaggregation, EC allows for broad tunability of ink viscosity to enable compatibility with diverse printing methods ranging from low-viscosity inkjet printing to high-viscosity blade coating. The polymer stabilizer also imparts porosity to the final printed structure since EC is largely volatilized upon thermal curing, resulting in a porous hBN microstructure. Lastly, the thermal volatilization of EC leaves behind

a nanoscale carbonaceous coating on the hBN nanosheets that promotes wetting by organic electrolytes and enhanced ionic conductivities, ultimately enabling lithium-ion battery cells based on printed hBN separators with improved rate capability and cyclability compared to traditional polymer-based battery separators.

## 2. Results and Discussion

### 2.1. Viscosity-Tunable hBN Inks

The hBN nanosheets were prepared by liquid-phase shear exfoliation in the presence of EC as a polymer stabilizer. Specifically, a solution of 150 mg mL<sup>−1</sup> bulk hBN powder in 1.5 w/v% EC/ethanol was shear mixed for 120 min, followed by a centrifugation step to sediment out large, unexfoliated hBN particles. Flocculation of the hBN/EC solid was induced by addition of a saline solution to the supernatant of the sedimentation process to promote aggregation of hBN/EC particles, which were then isolated by centrifugation. The supernatant containing excess EC and ethanol was then discarded, and the flocculated hBN/EC solid was rinsed with deionized water until no measurable salt concentration was detected. The wet solids were then dried in ambient conditions, yielding a white powder composed of 90 wt% hBN and 10 wt% EC (Figures S1 and S3, Supporting Information).

Successful exfoliation of hBN nanosheets was confirmed with scanning electron microscopy (SEM, **Figure 1a**), which reveals the absence of large hBN particles. Individual hBN nanosheets were also observed by tapping mode atomic force microscopy (AFM) (**Figure 1b**), showing an average thickness of  $2.4 \pm 1.2$  nm ( $N = 107$ ) and sub-100 nm lateral dimensions that are compatible with inkjet printing without nozzle clogging.<sup>[38]</sup> Transmission electron microscopy (TEM) confirms the sub-100 nm lateral dimensions of the hBN nanosheets (**Figure 1c**) and reveals the nanoscale carbonaceous coating on the hBN nanosheet surface (**Figure 1d**).

The exfoliated hBN nanosheets are readily dispersed in a wide range of solvents, allowing for the preparation of diverse hBN ink formulations. In particular, inkjet printing requires that inks are readily jetted into well-defined droplets that result in high-resolution printed lines.<sup>[39]</sup> An inkjet printable (IJP) hBN ink was thus tailored to achieve a viscosity and surface tension consistent with the formation of stable droplets.<sup>[37]</sup> Specifically, the exfoliated hBN/EC powder was dispersed in a mixture of cyclohexanone and terpineol, yielding an IJP ink with a solid concentration of 5.1 wt% hBN and viscosity of  $8.0 \times 10^{-3}$  Pa s at 1000 s<sup>−1</sup> (**Figure 2a,c**).

Blade coating is an alternative additive manufacturing method that is more suitable for large-area thin-film coatings than IJP. In this case, the film thickness is controlled by

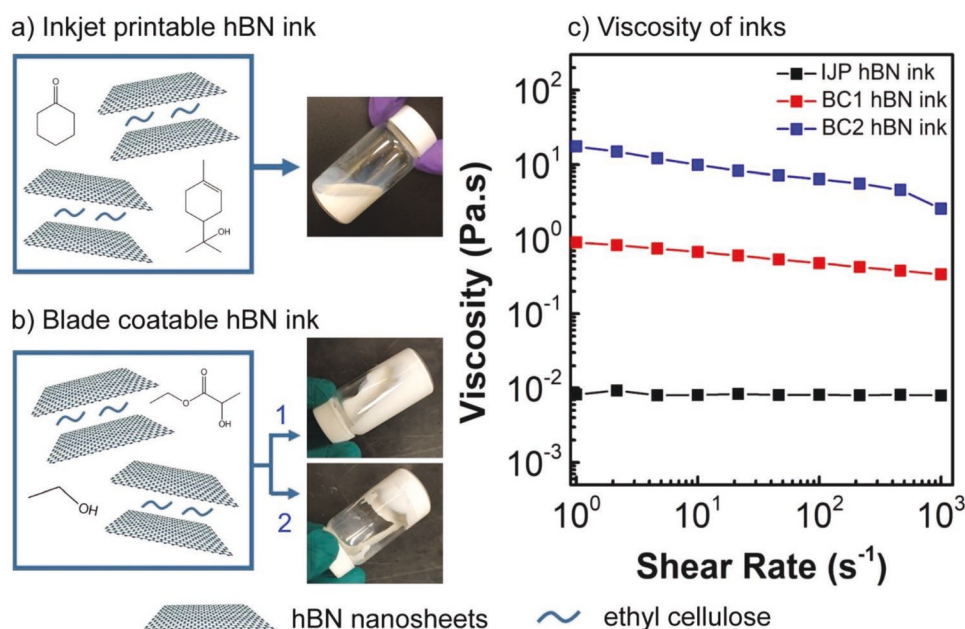


**Figure 2.** Ink preparation and rheological characterization. a) The IJP hBN ink is prepared by dispersion of the hBN/EC exfoliated powder in a 85:15 ratio of cyclohexanone and terpineol. b) BC hBN inks are prepared by dispersing hBN/EC powder in a 2:1 ratio of ethanol and ethyl lactate. The solvents are then evaporated to tune the viscosity, resulting in a low-viscosity BC1 hBN ink ( $0.4 \text{ Pa s}$  at  $10^3 \text{ s}^{-1}$ ) and a high-viscosity BC2 hBN ink ( $2.6 \text{ Pa s}$  at  $10^3 \text{ s}^{-1}$ ). c) Viscosity as a function of shear rate for all three hBN ink formulations.

adjusting the gap size of the blade to the substrate, allowing for the casting of films with thicknesses ranging from hundreds of nanometers to several microns.<sup>[40]</sup> A lower boiling point solvent system was utilized for the blade-coatable (BC) hBN ink, which consisted of a 2:1 mixture of ethanol and ethyl lactate. The as-prepared ink (BC1 hBN ink) possessed a solid concentration of 23 wt% and a viscosity of  $0.4 \text{ Pa s}$  at  $1000 \text{ s}^{-1}$  (Figure 2b-1,c), which is two orders of magnitude higher than the IJP ink. An additional higher viscosity ink (BC2 hBN ink) was prepared by partial evaporation of the solvents, resulting in a 45 wt% solid content and a viscosity of  $2.6 \text{ Pa s}$  at  $1000 \text{ s}^{-1}$  (Figure 2b-2,c). As shown in Figure 2c, the rheological properties of these inks show a pseudoplastic behavior, particularly for the BC2 ink. The observed shear-thinning behavior is expected for composite fluids whose viscosity decreases with a corresponding increase in shear rate.<sup>[26,30]</sup>

## 2.2. Inkjet Printable hBN Ink

The inkjet printability of the IJP hBN ink is demonstrated in Figure 3. The optical microcopy image (Figure 3a) shows highly uniform printed lines with well-defined edges. SEM imaging in Figure 3b,c presents additional evidence of the uniformity of the printed lines and the morphology of the hBN nanoflakes. The homogenous morphology of the printed lines confirms the quality of the IJP hBN ink formulation, which evidently minimizes coffee ring formation and other artifacts that can emerge during solvent evaporation.<sup>[41]</sup> In addition, it is notable that a single printing pass achieves sufficient thickness and uniformity for many applications due to the relatively high solid content of hBN. Patterning over large areas is illustrated in

Figure S4 of the Supporting Information, confirming the reliability of inkjet printing on diverse substrates such as glass and polyimide.

Multiple printing passes result in thicker lines where the average height increases linearly with the number of printing passes (Figure 3d). In particular, each additional printing pass adds  $204 \pm 5 \text{ nm}$  in thickness to the hBN patterns prior to annealing. Following thermal decomposition of the polymer dispersant, the average thickness of a single-pass line decreases to  $120 \pm 12 \text{ nm}$  (Figure 3e). Figure 3f provides optical profilometry height profiles after 1 and 5 passes, which corroborate the decrease in thickness after thermal annealing. The resulting printed patterns also show no evidence of delamination or cracking, demonstrating high mechanical integrity that is critical for subsequent processing and applications.

## 2.3. Blade-Coatable hBN Inks

### 2.3.1. Ion-Conductive hBN Inks

The results for the BC hBN inks are summarized in Figure 4. Following blade coating onto stainless steel substrates using a blade gap of  $22 \mu\text{m}$ , the BC1 and BC2 hBN inks resulted in smooth and homogeneous films with thicknesses of  $19.5 \pm 1.3$  and  $31.3 \pm 2.5 \mu\text{m}$ , respectively. As expected, the film thickness of the blade-coated films depends on the total solid concentration of the ink, where higher solid content leads to thicker films for a given blade gap. After blade coating, the films are dried at room temperature overnight, followed by thermal annealing at  $300^\circ\text{C}$  for 30 min to decompose the



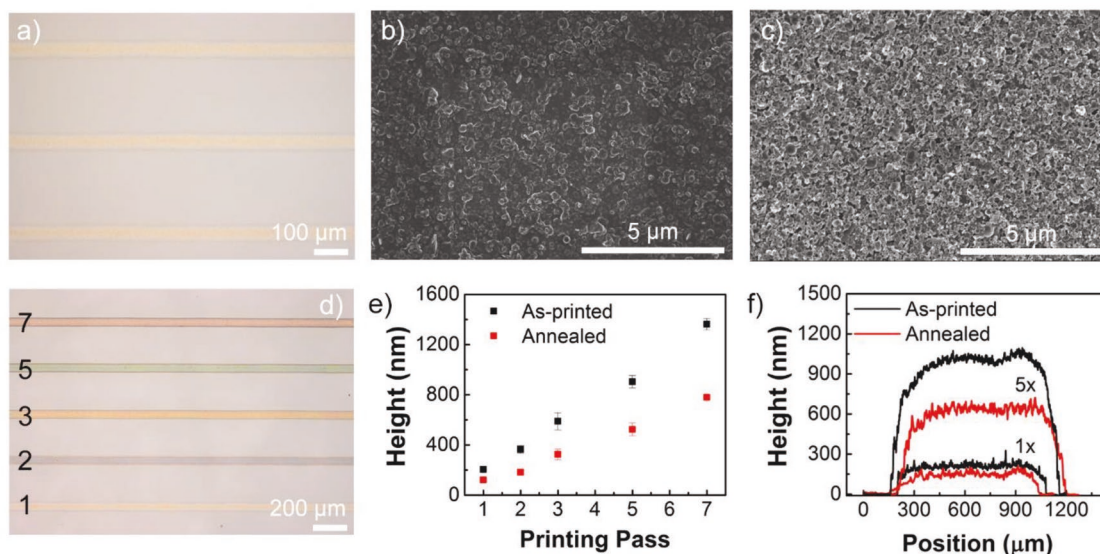


**Figure 3.** Inkjet printing results. a) Optical microscopy image of inkjet-printed hBN lines on a glass substrate. b, c) SEM images reveal the uniformity of the printed features, illustrating the percolating morphology of the hBN nanoflakes b) before and c) after thermal annealing. d) Optical microscopy image after multiple printing passes on a glass substrate. e) Average height of the hBN lines as-printed and following thermal annealing. f) Averaged cross-sectional profiles of the printed lines after 1 and 5 printing passes, demonstrating the increase in thickness after multiple printing passes and the decrease in thickness after thermal annealing.

EC polymer. The resulting surface morphology was examined by SEM as shown in Figure 4. The blade-coated thin films are comprised of well-stacked hBN nanosheet networks with the nanosheets mostly aligned in the plane of the substrate. The observed preferential horizontal orientation of the hBN nanosheets is consistent with previous reports for blade-coated graphene films.<sup>[36]</sup> In addition, the blade-coated hBN films possess uniform porosity after thermal volatilization of the EC polymer stabilizer.

Characterization of the chemical composition of the as-coated and thermally annealed hBN films was performed by X-ray photoelectron spectroscopy (XPS). The relative atomic percentages of carbon, oxygen, boron, and nitrogen obtained from XPS survey scans are shown in Figure 4e. Both as-coated hBN films show evidence of the presence of the EC polymer, including high atomic percentages of C and O. The low relative content of B and N also reflects the large presence of the polymer dispersant in the as-coated films. However, following annealing, the C and O content is drastically reduced, and the relative content of B and N is correspondingly increased, indicating successful polymer decomposition. The high-resolution C 1s spectra further show that the carbonaceous components of the hBN films were altered following thermal annealing (Figure 4f, g). Specifically, the C 1s spectra can be deconvoluted into three components that are assigned to C–C ( $\approx 285$  eV), C–O ( $\approx 287$  eV), and O–C=O ( $\approx 289$  eV), leading to the conclusion that the thermal decomposition of the EC polymer results in carbonaceous residues composed primarily of C–C and C–O bonds.

The carbon coating on the hBN nanosheets enhances wettability toward organic electrolytes including those commonly employed in lithium-ion batteries. **Figure 5** compares the organic electrolyte wettability of blade-coated hBN films to that of a commercial lithium-ion battery separator (Celgard). When

a droplet of organic electrolyte is placed on the surface of the blade-coated hBN film, it rapidly infiltrates the interior porous microstructure, resulting in complete wetting within 10 s. By contrast, the commercial separator shows considerably less wetting under the same testing conditions. High wettability is an essential property for a battery separator to efficiently transport ions between the electrodes and minimize the cell impedance. In addition, efficient wetting reduces the time required for electrolyte filling, which simplifies manufacturing and extends the battery life cycle.<sup>[42]</sup>

Porosity is another critical characteristic of a separator material since it facilitates ion transport and leads to enhanced ionic conductivity. SEM images (Figure 4a–d) reveal an interconnected porous microstructure of hBN films with the blade-coated BC1 and BC2 hBN films showing a porosity of 60% and 69%, respectively. For context, the commercially available separator displayed a lower porosity of 38% (Figure 5d). With high porosity and organic electrolyte wettability, the blade-coated hBN films possess ionic conductivity values in excess of  $1 \text{ mS cm}^{-1}$ , which outperforms the commercial separator by more than a factor of two at room temperature (Figure 5d). Measurements of the temperature dependence of ionic conductivity show the expected behavior of increasing ionic conductivity with increasing temperature (Figure S9, Supporting Information).<sup>[43]</sup>

The thermal properties of the hBN films are compared to the commercial polymer-based separator in Figure 5e. Following heating to  $150^\circ\text{C}$  for 10 min on a hot plate, the commercial separator loses mechanical integrity and undergoes significant shrinkage, whereas the hBN films remained intact. This improved thermal stability results from the polymer-free composition of the annealed blade-coated hBN films and the superlative thermal and chemical stability of hBN nanosheets, which are stable up to  $1000^\circ\text{C}$  in oxidizing environments.<sup>[44]</sup>

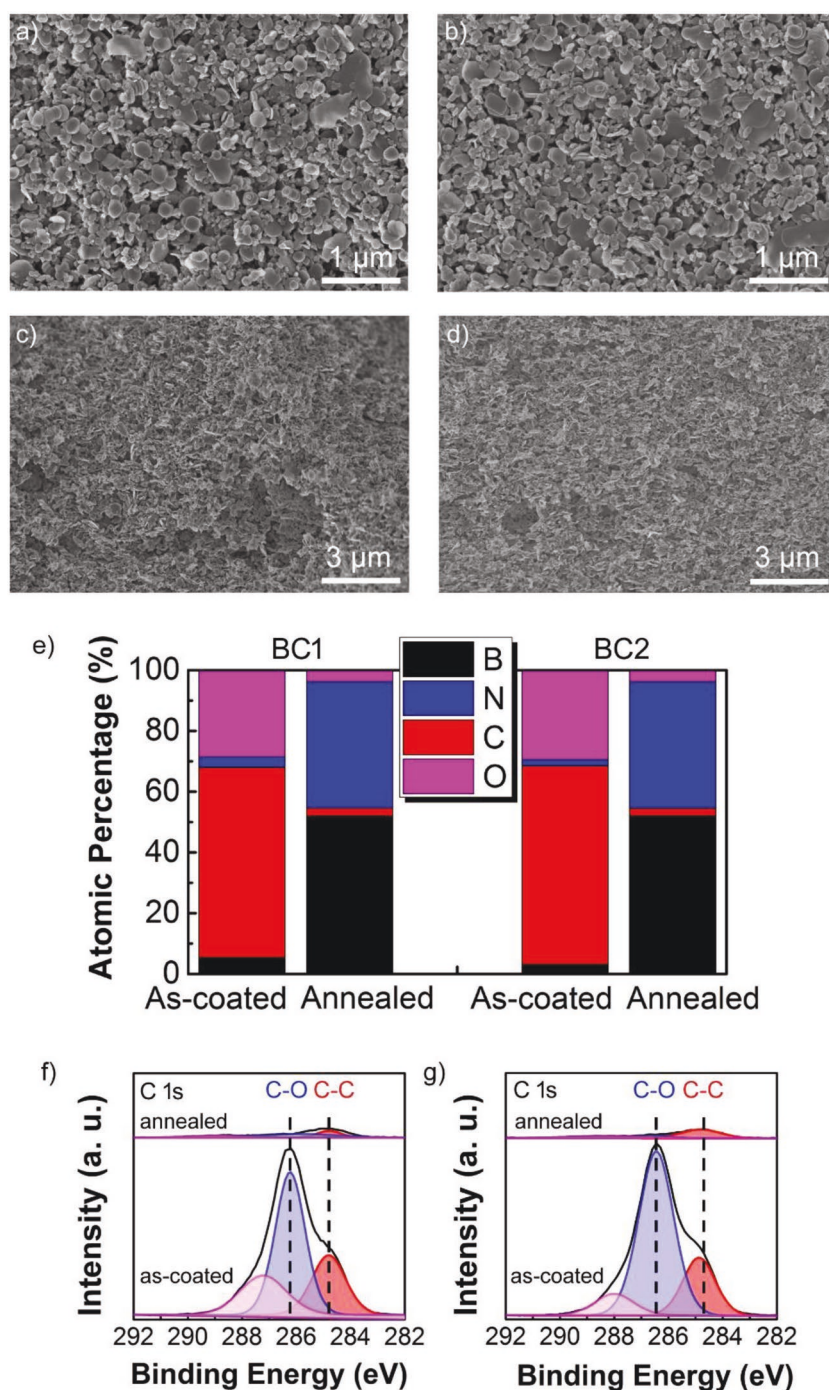


**Figure 4.** Blade coating results. SEM images of a,c) low-viscosity and b,d) high-viscosity BC hBN inks. SEM images were captured at the (a,b) top surface and (c,d) cross-sections of the hBN films. e) Atomic composition of the as-coated and annealed hBN films prepared from low-viscosity (BC1) and high-viscosity (BC2) hBN inks. f,g) High-resolution C 1s XPS scan for the (f) low-viscosity and (g) high-viscosity hBN inks as-coated and after annealing.

This thermal stability underscores the utility of hBN films for applications where thermal runaway must be minimized, such as lithium-ion batteries in consumer electronics or electric vehicles.

### 2.3.2. Lithium-Ion Batteries Based on Printed hBN Separators

The suitability of the blade-coated hBN films for separators in a lithium-ion battery was assessed by the electrochemical performance of half-cell assemblies comprised of lithium manganese oxide (LMO)–graphene cathode electrodes and 1.0 M LiPF<sub>6</sub> in ethylene carbonate/diethyl carbonate (EC/DEC) (50/50 (v/v)) liquid electrolyte. The lithium-ion battery cells were assembled by blade-coating the binder-free LMO–graphene electrode onto an aluminum foil substrate followed by blade-coating the hBN ink onto the electrode surface, resulting in smooth and homogeneous hBN films with a thickness of 20 μm. Subsequently, the printed structure was subjected to thermal annealing to decompose the EC polymer and create the nanoporous hBN network.

The electrochemical performance of the LMO–graphene|hBN|Li battery cells was first evaluated by conducting cycling stability measurements at a current rate of 0.5C for 100 cycles. **Figure 6a** demonstrates that the blade-coated hBN separator showed improved performance in comparison to a commercial Celgard separator throughout the entire test, exhibiting superior capacity retention of 82% after 100 cycles. **Figure 6b** presents rate capability tests with current rates ranging from 0.2C to 15C for the blade-coated hBN separator in comparison to a commercial Celgard separator. The blade-coated hBN separator resulted in higher capacity at each current rate, outperforming the commercial Celgard separator at all tested current rates with particularly noteworthy performance at elevated current rates. The corresponding charge–discharge voltage profiles in **Figure 6c,d** show that the blade-coated hBN separator displayed capacities of 109 and 41 mAh g<sup>−1</sup> at 0.2C and 15C, respectively, while the Celgard separator battery cell capacities dropped to 99 and 4 mAh g<sup>−1</sup> at 0.2C and 15C, respectively. The excellent cycling stability and rate performance of the lithium-ion battery cells based on the printed hBN separator can be attributed to the high porosity, wettability, and ionic conductivity of the hBN films, which promote fast lithium ion diffusion kinetics and enhanced lithium ion transport.

## 3. Conclusion

In summary, we have demonstrated a scalable, polymer-stabilized method for liquid-phase hBN exfoliation and



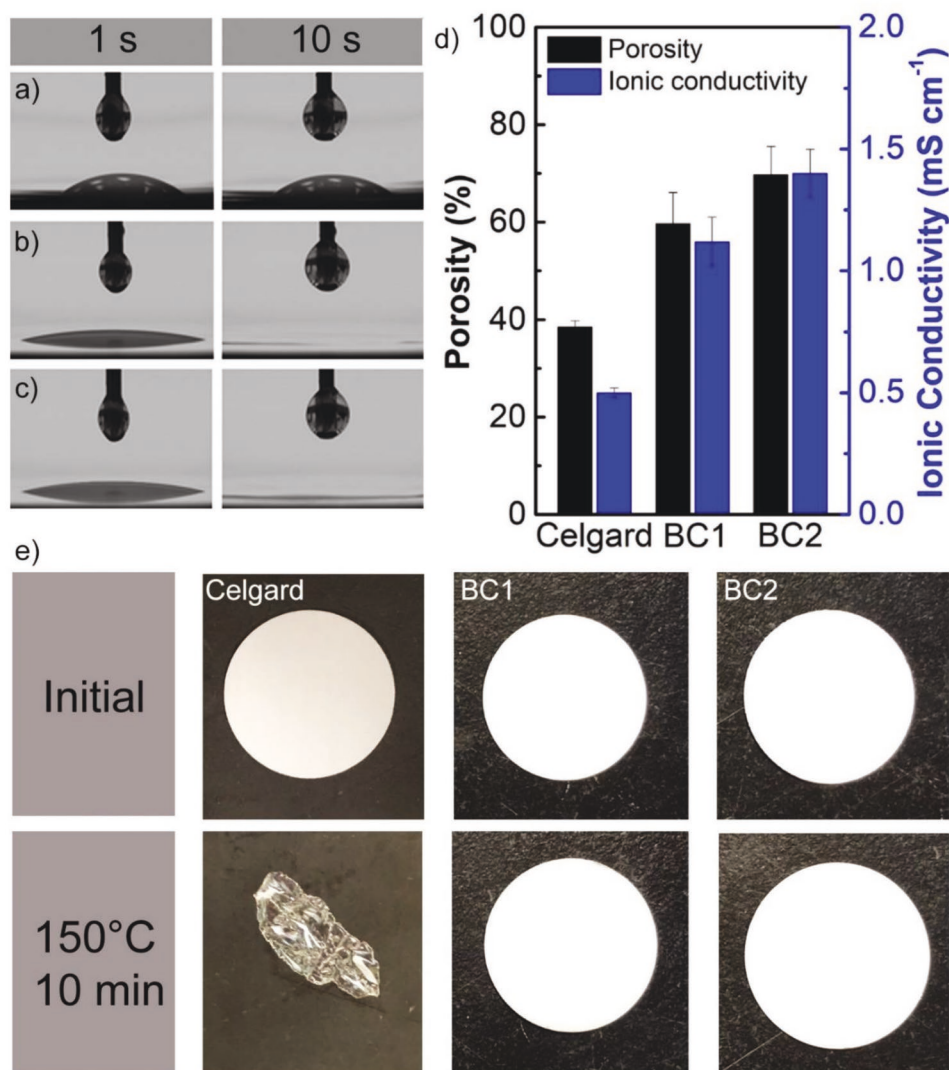


**Figure 5.** Comparison of hBN films to commercial Celgard lithium-ion battery separators. a–c) Contact angle measurements to assess organic electrolyte wettability of (a) Celgard, (b) blade-coated BC1 hBN film, and (c) blade-coated BC2 hBN film. In particular, a 5  $\mu\text{L}$  liquid electrolyte drop (1.0 M LiPF<sub>6</sub> in EC/DEC (50/50 (v/v))) was deposited on the surface of each film and photographs were taken after 1 and 10 s. d) Room temperature ionic conductivity and porosity measurements of Celgard and hBN films. e) Thermal properties of the Celgard and hBN films. Photographs were taken after the heating samples on a hot plate for 10 min at  $150^\circ\text{C}$ . The hBN films show no change, whereas the Celgard film undergoes dramatic morphological changes and shrinkage.

printable ink formulation. By controlling the ink rheology through choice of solvent system and EC loading, hBN nanosheets were successfully deposited by inkjet printing to create uniform, patterned lines on a variety of substrates. Moreover, due to the broad viscosity tunability of EC-stabilized hBN nanosheets, BC hBN inks were also demonstrated for large-area applications. Following thermal annealing, the EC polymer is largely volatilized, resulting in high porosity films where the hBN nanosheets possess a carbonaceous coating that promotes organic electrolyte wettability. The combination of high porosity and organic electrolyte wettability leads to high ionic conductivity that competes favorably with commercial lithium-ion battery separators. In addition, the high thermal and chemical stability of hBN provides additional advantages by maintaining mechanical integrity at elevated temperatures, which helps

mitigate thermal runaway concerns in lithium-ion batteries. Finally, the electrochemical performance of battery cells based on printed hBN separators exhibited rate capability and cycling stability results that exceeded commercial polymer separators. Overall, this work establishes a series of viscosity-tunable hBN inks with high ionic conductivity that present promising opportunities for next-generation printed electronics and energy storage technologies.

#### 4. Experimental Section

*Hexagonal Boron Nitride Exfoliation, Processing, and Characterization:* 120 g of bulk hBN flakes (Sigma-Aldrich) were dispersed in an 800 mL solution of EC (viscosity 4 cP, Sigma-Aldrich) dissolved in ethanol (0.015 g mL<sup>-1</sup>, Decon Labs, 200 proof grade) and placed in a stainless

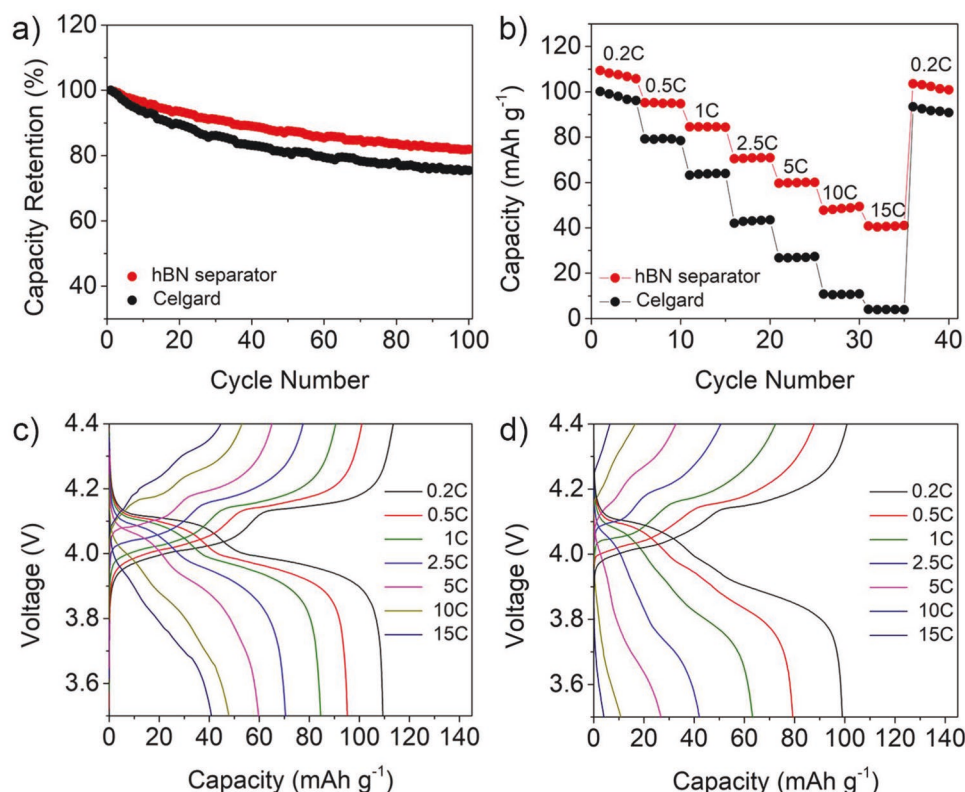


**Figure 6.** Electrochemical performance of printed LMO-graphene|hBN|Li battery cells in comparison to equivalent battery cells constructed with a commercial Celgard separator. a) Cycling stability performance at 0.5C. b) Rate capability measurements from 0.2C to 15C. c,d) Charge-discharge voltage profiles at different current rates for (c) blade-coated hBN separator and (d) Celgard separator.

steel beaker. The mixture was shear mixed (laboratory shear mixer model L5M-A, Silverson) for 120 min at maximum speed (10 230 rpm) to exfoliate the hBN nanosheets. The resulting dispersion was centrifuged at 4000 rpm for 20 min to sediment out large particles (Avanti J-26 XPI centrifuge, JS 7.5 rotor, Beckman Coulter). The supernatant containing ethanol, EC, and hBN nanosheets was collected. To remove excess EC and solvent, a flocculation method was employed. In this step, the supernatant was mixed with an aqueous sodium chloride solution (0.04 mg mL<sup>-1</sup> NaCl, Sigma-Aldrich) in a 16:9 weight ratio and centrifuged for 6 min at 7500 rpm to sediment the exfoliated hBN/EC. The sediment was washed with deionized water to remove residual salt and dried to yield the exfoliated hBN/EC powder (Figure S1, Supporting Information).

Thermogravimetric analysis (TGA) was performed on the resulting powder, which revealed an hBN solid content of 90 wt%. The TGA measurement was conducted over a temperature interval from 25 to 600 °C with a ramp of 10 °C min<sup>-1</sup> under a synthetic air flow rate of 50 mL min<sup>-1</sup> (Mettler Toledo TGA/SDTA851). SEM (Hitachi SU8030 microscope operating at 2 kV) was performed on samples coated with a 7 nm thick layer of osmium tetroxide using a hollow cathode osmium plasma coater (model OPC-60A, Structure Probe, Inc.). The EC coating on the hBN nanosheets was confirmed by TEM carried out on a JEOL JEM-2100 microscope at an accelerating voltage of 200 kV. Tapping mode AFM imaging of the hBN nanosheets was performed on an Asylum Research Cypher AFM with a Nanoworld NCHR probe. The sample was prepared by dropping a diluted dispersion of hBN/EC in ethanol onto a previously cleaned Si/SiO<sub>2</sub> wafer.

**Inks Preparation and Characterization:** For inkjet printing, hBN/EC powder and EC (viscosity 4 cP, Sigma-Aldrich) were dispersed in 85:15 v/v cyclohexanone/terpineol (Sigma-Aldrich) by bath sonication for 6 h. The dispersion was further filtered through a 3.1 µm glass fiber membrane (Whatman syringe filter) to prevent clogging of the inkjet nozzles,

yielding an ink with 5.1 wt% hBN solid loading and viscosity of  $8.0 \times 10^{-3}$  Pa s at 1000 s<sup>-1</sup>. Inkjet printing was performed with a Ceradrop X-Series inkjet printer equipped with a 10 µL nominal drop size Dimatix cartridge (DMC-11610) using a Dimatix Model Fluid 2 waveform jetting parameter with the inkjet nozzle plate and substrate maintained at 30 °C. Glass slides (Fisherbrand, 1 mm thick) and polyimide films (DuPont Kapton, 125 µm thick) served as substrates and were used as received. Lateral resolution of the printed patterns was observed by optical microscopy (Olympus Optical Microscope) and SEM (Hitachi SU8030). Thicknesses measurements of the inkjet-printed lines were obtained using a Dektak 150 Stylus Surface Profiler.

BC hBN inks were prepared by mixing exfoliated hBN/EC powder, EC (viscosity 4 cP, Sigma-Aldrich), ethanol (Decon Labs, 200 proof), and ethyl lactate (Sigma-Aldrich) by bath sonication for 6–8 h. The dispersion was heated on a hot plate to evaporate ethanol, producing an ink with 23 wt% solid content in ethyl lactate and a viscosity of 0.4 Pa s at 1000 s<sup>-1</sup>. Further evaporation of solvents resulted in a higher viscosity BC hBN ink, with 45 wt% solid content in ethyl lactate and a viscosity of 2.6 Pa s at 1000 s<sup>-1</sup>. The shear viscosity of all inks was measured using an Anton Paar Physica MCR 302 rheometer equipped with a 25 mm, 2° cone and plate geometry at shear rates from 1 s<sup>-1</sup> to 1000 s<sup>-1</sup> at 25 °C.

For blade coating, the hBN inks were deposited onto stainless steel disk substrates by dragging the film casting knife (EQ-Se-KTQ-50 film applicator with adjustable micrometer) using an automatic film coater (model MSK-AFA-III) at a speed of  $\approx 20$  cm s<sup>-1</sup>, producing homogeneous films with consistent thicknesses. hBN films were allowed to dry at room temperature overnight followed by thermal annealing at 300 °C for 30 min under ambient air conditions in a tube furnace (Lindberg Blue M, Thermo Fisher Scientific). SEM (Hitachi SU8030) images of hBN film surfaces and cross-sections were used to examine the resulting morphology. XPS measurements were performed on an ESCALAB 250

XI<sup>+</sup> spectrometer (Thermo Fisher Scientific) equipped with an electron flood gun and a scanning ion gun. Analysis of XPS data was performed using the Thermo Advantage software. The wettability of the blade-coated hBN films was estimated by a video contact angle system (VCA Optima). The measurements were carried out by dropping 5  $\mu$ L liquid electrolyte (1.0 M LiPF<sub>6</sub> in EC/DEC (50/50 (v/v)), battery grade, Sigma-Aldrich) on the hBN film surfaces. Image capture was recorded using Dynamic-2500 software at a rate of 60 frames per s. The porosity of the hBN films was measured by the *n*-butanol absorption method.<sup>[45]</sup> In this approach, hBN films were weighed before and after immersion in *n*-butanol (Sigma-Aldrich) for 1 h. The porosity was then calculated using Equation (1)

$$\text{Porosity (\%)} = \frac{w_1 - w_0}{\rho \times V} \times 100 \quad (1)$$

where  $w_1$  and  $w_0$  are the weight of wet and dry hBN films, respectively,  $\rho$  is the density of *n*-butanol, and  $V$  is the geometric volume of the hBN film.

The ionic conductivity of the hBN films was measured by electrochemical impedance spectroscopy (EIS). For the assembly of cells used in the ionic conductivity measurements, a blade-coated hBN film on a stainless-steel disk was wetted with liquid electrolyte (1.0 M LiPF<sub>6</sub> in EC/DEC (50/50 (v/v)), Sigma-Aldrich) and then sandwiched with another stainless steel disk electrode of equal size (area = 1.86 cm<sup>2</sup>). The cells were allowed to age overnight prior to electrochemical measurements. Temperature-dependent measurements were carried out using an environmental chamber (model BTL-433, ESPEC) to precisely control sample temperature in the range from –10 to 50 °C. The cells were allowed to equilibrate for 30 min at each temperature before the measurement was recorded. Electrochemical measurements were performed using a potentiostat/galvanostat/EIS model SP-300 (Bio-Logic Science Instruments), applying an AC amplitude of 10 mV over a frequency range from 0.1 Hz to 1 MHz. The ionic conductivity ( $\sigma$ ) of the hBN films was calculated using Equation (2)

$$\sigma = \frac{t}{R \times A} \quad (2)$$

where  $t$  corresponds to the thickness of the hBN film,  $R$  is the resistance determined from EIS, and  $A$  is the area of the stainless-steel electrode.

**Electrode Preparation:** Binder-free LMO–graphene electrodes were prepared following a previously established method.<sup>[46]</sup> The slurry was prepared by dispersing LMO active material (LiMn<sub>2</sub>O<sub>4</sub>, spinel, NEI Corporation) and graphene/EC powder in *N*-methyl-2-pyrrolidone (anhydrous, Sigma-Aldrich) in a 9:1 weight ratio. The LMO–graphene/EC slurry was ultrasonicated for 3 h and subsequently blade-coated onto an aluminum substrate as current collector. The electrode sheets were dried in a vacuum oven at 80 °C overnight followed by thermal annealing at 265 °C for 1 h under ambient condition to decompose EC, resulting in a binder-free LMO–graphene cathode containing 90 wt% LMO and 10% conductive graphene additive. The graphene utilized to prepare these electrodes was produced by dispersing graphite (Sigma-Aldrich) powder in an ethanolic solution of EC (viscosity 4 cP, Sigma-Aldrich) in a 30:1:20 weight ratio. The solution was then shear mixed for 23 h using an inline mixer (200L, Silverson) equipped with a square hole screen. The resulting dispersion was centrifuged at 6500 rpm for 30 min (Avanti J-26 XPI centrifuge, JLA 8.1000 rotor, Beckman Coulter) to sediment out unexfoliated graphite flakes. The supernatant containing exfoliated graphene/EC was collected, flocculated with a 0.04 mg mL<sup>–1</sup> saline solution in a 16:9 weight ratio to remove excess EC, and centrifuged at 7000 rpm for 7 min to sediment the graphene/EC nanosheets. The isolated solid was washed with deionized water and dried in air to yield the exfoliated graphene/EC powder.

**Lithium-Ion Battery Assembly and Testing:** For the assembly of lithium-ion battery cells, the LMO–graphene electrodes were punched into 0.79 cm<sup>2</sup> disks, and the BC hBN ink (BC1 ink) was deposited onto the electrode surface by dragging the film casting knife to produce homogeneous films with consistent thicknesses of 20  $\mu$ m. The LMO–graphene/hBN films were allowed to dry at room temperature overnight followed by thermal annealing at 300 °C for

30 min under ambient air conditions in a tube furnace to remove EC. LMO–graphene/hBN|Li battery cells were assembled using the blade-coated hBN film as the separator and 1.0 M LiPF<sub>6</sub> in EC/DEC (50/50 (v/v), Sigma-Aldrich) as the electrolyte. Cycling performance tests were carried out using a BT-2143 battery cycler (Arbin Instruments) at a constant current rate of 0.5C for 100 cycles. Rate performance studies were tested for 5 cycles at 0.2C, 0.5C, 1C, 2.5C, 5 C, 10C, 15C, and 0.2C over a voltage range window of 3.5–4.4 V. Control cells were assembled using Celgard 2325 as the separator.

## Supporting Information

Supporting Information is available from the Wiley Online Library or from the author.

## Acknowledgements

A.C.M.M. acknowledges support provided by the Sao Paulo Research Foundation (FAPESP), Grant # 2017/15882-0. J.R.D. acknowledges support provided by the National Science Foundation Scalable Nanomanufacturing Program (NSF CMMI-1727846). The hBN ink development was primarily supported by MilliporeSigma. Electrochemical characterization was supported by the Center for Electrochemical Energy Science, an Energy Frontier Research Center funded by the U.S. Department of Energy (DOE), Office of Science, Basic Energy Sciences under Award # DEAC02-06CH1157. SEM, TEM, XPS, and profilometry were performed in the NUANCE facility at Northwestern University, which was supported by the Soft and Hybrid Nanotechnology Experimental (SHyNE) Resource (NSF ECCS-1542205), the Materials Research Science and Engineering Center (NSF DMR-1720139), and the State of Illinois, and Northwestern University. Rheometry and thermogravimetric analysis were performed in the MatCI facility which receives support from the NSF MRSEC Program (NSF DMR-1720139). Wettability tests were conducted at the Northwestern University Micro/Nano Fabrication Facility (NUFAB), which was supported by Soft and Hybrid Nanotechnology Experimental (SHyNE) Resource (NSF ECCS-1542205), the Materials Research Science and Engineering Center (DMR-1720139), the State of Illinois, and Northwestern University.

## Conflict of Interest

The IJP hBN ink and BC hBN ink are available commercially from MilliporeSigma as Product Nos. 901410 and 901349, respectively.

## Keywords

blade coating, ethyl cellulose, hBN, inkjet printing, liquid-phase exfoliation

Received: March 16, 2019

Revised: June 21, 2019

Published online: August 1, 2019

- [1] K. Novoselov, D. Jiang, F. Schedin, T. Booth, V. Khotkevich, S. Morozov, A. Geim, *Proc. Natl. Acad. Sci. USA* **2005**, 102, 10451.
- [2] H. Zhang, *ACS Nano* **2015**, 9, 9451.
- [3] J. Kang, V. K. Sangwan, J. D. Wood, M. C. Hersam, *Acc. Chem. Res.* **2017**, 50, 943.
- [4] A. K. Geim, K. S. Novoselov, *Nat. Mater.* **2007**, 6, 183.
- [5] C. N. R. Rao, A. K. Sood, K. S. Subrahmanyam, A. Govindaraj, *Angew. Chem., Int. Ed.* **2009**, 48, 7752.



- [6] C. Tan, X. Cao, X.-J. Wu, Q. He, J. Yang, X. Zhang, J. Chen, W. Zhao, S. Han, G.-H. Nam, M. Sindoro, H. Zhang, *Chem. Res.* **2017**, 117, 6225.
- [7] C. R. Dean, A. F. Young, I. Meric, C. Lee, L. Wang, S. Sorgenfrei, K. Watanabe, T. Taniguchi, P. Kim, K. L. Shepard, *Nat. Nanotechnol.* **2010**, 5, 722.
- [8] M. Wang, S. K. Jang, W.-J. Jang, M. Kim, S.-Y. Park, S.-W. Kim, S.-J. Kahng, J.-Y. Choi, R. S. Ruoff, Y. J. Song, S. Lee, *Adv. Mater.* **2013**, 25, 2746.
- [9] T. Roy, M. Tosun, J. S. Kang, A. B. Sachid, S. B. Desai, M. Hettick, C. C. Hu, A. Javey, *ACS Nano* **2014**, 8, 6259.
- [10] J. Zhu, J. Kang, J. M. Kang, D. Jariwala, J. D. Wood, J. W. T. Seo, K. S. Chen, T. J. Marks, M. C. Hersam, *Nano Lett.* **2015**, 15, 7029.
- [11] R. Worsley, L. Pimpolari, D. McManus, N. Ge, R. Ionescu, J. A. Wittkopf, A. Alieva, G. Basso, M. Macucci, G. Iannaccone, K. S. Novoselov, H. Holder, G. Fiori, C. Casiraghi, *ACS Nano* **2019**, 13, 54.
- [12] A. G. Kelly, D. Finn, A. Harvey, T. Hallam, J. N. Coleman, *Appl. Phys. Lett.* **2016**, 109, 023107.
- [13] F. Withers, H. Yang, L. Britnell, A. P. Rooney, E. Lewis, A. Felten, C. R. Woods, V. Sanchez Romaguera, T. Georgiou, A. Eckmann, Y. J. Kim, S. G. Yeates, S. J. Haigh, A. K. Geim, K. S. Novoselov, C. Casiraghi, *Nano Lett.* **2014**, 14, 3987.
- [14] D. Deepika, L. H. Li, A. M. Glushenkov, S. K. Hait, P. Hodgson, Y. Chen, *Sci. Rep.* **2015**, 4, 7288.
- [15] C. Zhi, Y. Bando, C. Tang, H. Kuwahara, D. Golberg, *Adv. Mater.* **2009**, 21, 2889.
- [16] W.-L. Song, P. Wang, L. Cao, A. Anderson, M. J. Mezzani, A. J. Farr, Y.-P. Sun, *Angew. Chem.* **2012**, 124, 6604.
- [17] C. Yuan, B. Duan, L. Li, B. Xie, M. Huang, X. Luo, *ACS Appl. Mater. Interfaces* **2015**, 7, 13000.
- [18] T. Morishita, N. Takahashi, *RSC Adv.* **2017**, 7, 36450.
- [19] J. Taha-Tijerina, T. N. Narayanan, G. Gao, M. Rohde, D. A. Tsentalovich, M. Pasquali, P. M. Ajayan, *ACS Nano* **2012**, 6, 1214.
- [20] F. Xiao, S. Naficy, G. Casillas, M. H. Khan, T. Katkus, L. Jiang, H. Liu, H. Li, Z. Huang, *Adv. Mater.* **2015**, 27, 7196.
- [21] L. Y. Niu, J. N. Coleman, H. Zhang, H. Shin, M. Chhowalla, Z. J. Zheng, *Small* **2016**, 12, 272.
- [22] V. Nicolosi, M. Chhowalla, M. G. Kanatzidis, M. S. Strano, J. N. Coleman, *Science* **2013**, 340, 1226419.
- [23] J. N. Coleman, M. Lotya, A. O'Neill, S. D. Bergin, P. J. King, U. Khan, K. Young, A. Gaucher, S. De, R. J. Smith, *Science* **2011**, 331, 568.
- [24] F. Bonaccorso, A. Lombardo, T. Hasan, Z. Sun, L. Colombo, A. C. Ferrari, *Mater. Today* **2012**, 15, 564.
- [25] J. Zhu, M. C. Hersam, *Adv. Mater.* **2017**, 29, 1603895.
- [26] F. Bonaccorso, A. Bartolotta, J. N. Coleman, C. Backes, *Adv. Mater.* **2016**, 28, 6136.
- [27] E. B. Secor, M. C. Hersam, *J. Phys. Chem. Lett.* **2015**, 6, 620.
- [28] Y. Aleeva, B. Pignataro, *J. Mater. Chem. C* **2014**, 2, 6436.
- [29] T. Carey, S. Cacovich, G. Divitini, J. Ren, A. Mansouri, J. M. Kim, C. Wang, C. Ducati, R. Sordan, F. Torrisi, *Nat. Commun.* **2017**, 8, 1202.
- [30] A. M. Joseph, B. Nagendra, E. Bhoje Gowd, K. P. Surendran, *ACS Omega* **2016**, 1, 1220.
- [31] A. M. Gaikwad, D. A. Steingart, T. N. Ng, D. E. Schwartz, G. L. Whiting, *Appl. Phys. Lett.* **2013**, 102, 233302.
- [32] A. M. Gaikwad, A. C. Arias, D. A. Steingart, *Energy Technol.* **2015**, 3, 305.
- [33] A. J. Blake, R. R. Kohlmeier, J. O. Hardin, E. A. Carmona, B. Maruyama, J. D. Berrigan, H. Huang, M. F. Durstock, *Adv. Energy Mater.* **2017**, 7, 1602920.
- [34] V. Deimede, C. Elmasides, *Energy Technol.* **2015**, 3, 453.
- [35] Y. T. Liang, M. C. Hersam, *J. Am. Chem. Soc.* **2010**, 132, 17661.
- [36] E. B. Secor, T. Z. Gao, A. E. Islam, R. Rao, S. G. Wallace, J. Zhu, K. W. Putz, B. Maruyama, M. C. Hersam, *Chem. Mater.* **2017**, 29, 2332.
- [37] E. B. Secor, B. Y. Ahn, T. Z. Gao, J. A. Lewis, M. C. Hersam, *Adv. Mater.* **2015**, 27, 6683.
- [38] P. Calvert, *Chem. Mater.* **2001**, 13, 3299.
- [39] B. E. Kahn, *Proc. IEEE* **2015**, 103, 497.
- [40] Y.-H. Chang, S.-R. Tseng, C.-Y. Chen, H.-F. Meng, E.-C. Chen, S.-F. Horng, C.-S. Hsu, *Org. Electron.* **2009**, 10, 741.
- [41] E. B. Secor, P. L. Prabhumirashi, K. Puntambekar, M. L. Geier, M. C. Hersam, *J. Phys. Chem. Lett.* **2013**, 4, 1347.
- [42] X. Huang, *J. Solid State Electrochem.* **2011**, 15, 649.
- [43] P. Raghavan, X. Zhao, J.-K. Kim, J. Manuel, G. S. Chauhan, J.-H. Ahn, C. Nah, *Electrochim. Acta* **2008**, 54, 228.
- [44] N. Kostoglou, K. Polychronopoulou, C. Rebholz, *Vacuum* **2015**, 112, 42.
- [45] J. Ding, Y. Kong, P. Li, J. Yang, *J. Electrochem. Soc.* **2012**, 159, A1474.
- [46] K.-S. Chen, R. Xu, N. S. Luu, E. B. Secor, K. Hamamoto, Q. Li, S. Kim, V. K. Sangwan, I. Balla, L. M. Guiney, J.-W. T. Seo, X. Yu, W. Liu, J. Wu, C. Wolverton, V. P. Dravid, S. A. Barnett, J. Lu, K. Amine, M. C. Hersam, *Nano Lett.* **2017**, 17, 2539.